Current Research in Microbial Sciences 8 (2025) 100376

Contents lists available at ScienceDirect

Current Research in Microbial Sciences

journal homepage: www.sciencedirect.com/journal/current-research-in-microbial-sciences

Novel peptide inhibitor for the Chikungunya virus nsP2 protease: Identification and characterization

Mohammadamin Mastalipour [a], Ian Gering [b], Mônika Aparecida Coronado [a,b], Jorge Enrique Hernández González [c], Dieter Willbold [a,b], Raphael Josef Eberle [d,*]

[a] Institut für Physikalische Biologie, Heinrich-Heine-Universität Düsseldorf, Universitätsstraße 1, 40225 Düsseldorf, Germany
[b] Institut für Biologische Informationsprozesse, Strukturbiochemie (IBI-7), Forschungszentrum Jülich, 52425 Jülich, Germany
[c] São Paulo State University (UNESP), Institute of Biosciences, Humanities and Exact Sciences, São José do Rio Preto, Brazil
[d] Institut für Biochemische Pflanzenphysiologie, Heinrich-Heine-Universität Düsseldorf, Universitätsstraße 1, 40225 Düsseldorf, Germany

ARTICLE INFO

Keywords:
Chikungunya virus
nsP2 protease
Peptide inhibitor

ABSTRACT

Chikungunya virus (CHIKV) is an emerging pathogen affecting populations worldwide, with rapidly increasing infection rates. CHIKV, an arbovirus of the alphavirus genus, is predominantly found in tropical regions and transmitted by *Aedes* mosquitoes. Climate change has accelerated the global spread of these vectors, leading to outbreaks in non-tropical regions, including parts of Europe. The absence of antiviral therapies and the potential for co-infections with other viruses make CHIKV a significant public health concern. CHIKV replication relies on nsP2 cysteine protease activity to cleave its viral polyprotein into functional nonstructural and structural proteins. Targeting the nsP2 protease represents a promising strategy for antiviral therapy development. In this study, phage display was used to screen a library of peptides for potential binders of the target protease. Biophysical and biochemical analyses of the identified peptides assessed their inhibitory potential. Among the six identified peptides (named as P1–P6), four demonstrated inhibitory effects on the nsP2 protease (nsP2^{pro}). Peptide P1 exhibited the strongest inhibitory effect, with a half-maximal inhibitory concentration (IC$_{50}$) of 4.6 ± 1.9 μM, and a low cytotoxicity. The secondary structure analysis through CD spectroscopy and homology modelling revealed that P1 adopts an alpha-helical conformation. Finally, molecular dynamics simulations enabled us to investigate the dynamics of the nsP2^{pro} active site and molecular docking was employed to predict the orthosteric binding mode of P1, providing insights into protein-peptide interaction. These findings underscore the potential of peptide P1 as a lead compound for further investigation in the context of CHIKV research.

1. Introduction

Changes in environmental, climatic, and ecological conditions create favorable environments for the proliferation of arthropod-borne viruses, affecting nations worldwide (El-Sayed and Kamel, 2020). The lack of awareness, combined with underinvestment in fragile health systems and scientific research, results in a scarcity of effective antiviral medications (Mayer et al., 2017), complicating disease control efforts. Chikungunya fever is a re-emerging disease that has spread across the globe (Mourad et al., 2022). The infection can cause in the acute phase a variety of clinical symptoms like fever, rash, muscle and joint pain, which can last for 7–10 days (Freppel et al., 2024; Rama et al., 2024). However, in the chronic phase, rheumatoid arthritis and chronic pain can occur (Marimoutou et al., 2015; Paixao et al., 2018; Zaid et al., 2018).

Chikungunya virus (CHIKV) is the causative agent of CHIKV fever (Peinado, et al., 2022) and it has been reported in diverse regions including Africa, Asia, and Central and South America, where it continues to cause new infections (Grabenstein and Tomar, 2023). From 2013 to 2023, approximately 3.7 million confirmed CHIKV cases were reported in the Americas, with the World Health Organization (WHO) estimating that 3–5 million new infections occur annually (de Souza et al., 2024; Sharif et al., 2021). Additionally, data from the European Center for Disease Prevention and Control (ECDC) indicate that by November 2024, Brazil, Argentina, Paraguay, and Bolivia accounted for approximately 480,000 new cases and 190 fatalities (European Centre for Disease Prevention and Control [ECDC], 2024).

CHIKV is an arthropod-borne human pathogenic virus (Arbovirus), which is transmitted to humans by mosquitoes of the genus *Aedes aegypti*

---

* Corresponding author.
E-mail address: eberler@uni-duesseldorf.de (R.J. Eberle).

https://doi.org/10.1016/j.crmicr.2025.100376

(Delrieu et al., 2023; Simon et al., 2011). Besides CHIKV, other arboviruses, that belong to the flavivirus genus, such as Zika virus (ZIKV) and Dengue virus (DENV) share the same vector, potentially leading to co-infections that can result in complications like multi-organ dysfunction syndrome (Vikhe et al., 2023). Because these infections often present similar symptoms, misdiagnoses can occur and pose life-threatening risks; however, insufficient information is available to fully assess the outcomes of such co-infections (Ahmed et al., 2024; Khongwichit et al., 2022).

CHIKV belongs to the alphavirus genus and is a positive-sense single-stranded RNA virus whose genome encodes six structural proteins, including envelope proteins (E), capsid proteins, and four non-structural proteins (nsP1–4), which are vital for virus replication (Girard et al., 2024; Peinado et al., 2024; Solignat et al., 2009). The nsP2 protease (nsP2^{pro}), which is essential for viral proliferation, exhibits RNA triphosphatase and helicase activities in its N-terminus (Law et al., 2021). In contrast, its C-terminal region comprises two distinct functional domains: a cysteine protease domain and a methyltransferase-like domain. The cysteine protease domain plays a crucial role in cleaving the viral polyprotein P1234 into its functional proteins (Ghoshal et al., 2024; Merten et al., 2024; Silva and Dermody, 2017). The cysteine protease domain belongs to the papain superfamily, more precisely to the peptidase family C9 of clan CA (Rawlings et al., 2010). The alphavirus nsP2^{pro} structure uncovers a unique fold, distinct from other cysteine proteases. Nevertheless, the relative positioning of the catalytic Cys and His residues in the active site mirrors the catalytic arrangement seen in papain-like cysteine proteases (Narwal et al., 2018). The C-terminus methyltransferase-like domain of nsP2 is involved in suppressing interferon responses and disrupting MHC-I antigen presentation (Göertz et al., 2018; Ware et al., 2024).

For years, no vaccine was available for CHIKV, fortunately, a recently developed live-attenuated vaccine VLA1553 (IXCHIQ), has demonstrated safety and efficacy against CHIKV infections (Chen et al., 2024; Ly, 2024; Schneider et al., 2023). Although this vaccine represents a significant advance, its usefulness is limited for infected individuals. This factor highlights the ongoing need to develop antiviral drugs targeting CHIKV infections. Additionally, several studies described the usage of biologically active compounds, extracted from plants that possess an inhibitory effect against the virus protease including, hesperidin and thiazolidinone derivatives (Eberle et al., 2021; Jadav et al., 2015; Martins et al., 2024). However, no drug candidates or approved drugs targeting this protease have been reported to date.

Phage display is a widely used method for developing therapeutic drugs and diagnostics against various diseases, ranging from infectious diseases to neurodegenerative conditions like Alzheimer's. One promising drug, PRI-002, was originally identified through phage display screening and has shown significant potential in the treatment of Alzheimer's disease (Kutzsche et al., 2020; van Groen et al., 2017) . In 2020, it successfully passed its first phase of clinical trials. As mentioned, phage display can also be used to develop therapies against infectious diseases. Following the COVID-19 outbreak, researchers utilized phage display to identify peptides targeting the virus, e.g., targeting the main protease or the spike protein of SARS-CoV-2 (Sevenich et al., 2022; Eberle et al., 2023). Additionally, numerous studies have identified lead compounds and drug candidates through phage display, demonstrating its potential across various fields, including infectious diseases, neurodegenerative disorders, and cancer. Table 1 provides an overview of some of the different therapeutic agents identified using phage display, along with their respective target diseases. These findings highlight the effectiveness and versatility of phage display as a powerful tool for drug discovery and diagnostic development. In this manuscript, we employed phage display as an alternative strategy to identify peptide candidates targeting the CHIKV nsP2^{pro}. We successfully identified peptides that inhibit nsP2^{pro} activity in the micromolar range. Additionally, we demonstrated the low toxicity of the most promising peptide using the MTT assay, reinforcing its suitability as a lead compound for advancing CHIKV-related studies.

Table 1
Overview of therapeutic agents identified using phage display.

Agent(s)	Target	Reference
PRI-002	Aß-oligomeres (Alzheimer disease)	(Kutzsche et al., 2020; van Groen et al., 2017)
Peptide	Spike protein (SARS-CoV-2)	(Sevenich et al., 2022)
Peptide	Main protease (SARS-CoV-2)	(Eberle et al., 2023)
HER2, C5AR1	Breast cancer	(Yau et al., 2024)
Raxibacumab/ ABthrax®	Anthrax PA (*Bacillus anthracis*)	(Alfaleh et al., 2020)
V$_H$H (caplacizumab)	Blood clotting disorders	(Rossotti et al., 2023)

2. Materials and methods

2.1. Protein expression and purification

Protein expression and purification were carried out according to the method described in (Eberle et al., 2021) (Supplementary Fig. S1).

2.2. Phage display

The M13 bacteriophage library TriCo-16 (Creative Biolabs, Shirley, USA) was employed, offering a diversity of 2.6 × 10^{10} pIII-fused 16-mer peptide variants. The target protein was diluted in 10 mM sodium acetate buffer (pH 5.2) to 30 pM and added (100 μL) to a 96-well amino plate. Control wells received an immobilization buffer (10 mM sodium acetate, pH 5.2). The plate was incubated at room temperature (RT) for 30 min with shaking at 10 rpm. Binding was quenched by adding 200 μL of quenching buffer (1 M ethanolamine-HCl, pH 8.0) and incubating for 30 min, followed by the addition of 200 μL of blocking buffer (25 mM HEPES pH 7.4, 1 % (w/v) BSA) for another 30 min to block further binding. After washing the wells three times with wash buffer (25 mM HEPES, pH 7.4, 0.2 % BSA), 100 μL of the diluted phage library (1.66 × 10^{11} phages in 25 mM HEPES buffer) was added, and the mixture incubated for 20 min at RT. Unbound phages were removed by washing the wells five times.To elute bound phages, 100 μL of elution buffer (0.2 M glycine-HCl, pH 2.2) was added for 10 min at RT, and the eluted phages neutralized with 25 μL of neutralization buffer (1 M Tris-HCl, pH 9.1). To increase the specificity of the peptide binder, three rounds of selection were performed. After adding the phage in each round, Five-times washing step was carried out to remove nonspecific binders and those with low affinity.

2.2.1. Amplification and isolation of phages

120 μL of eluted phages were added to 20 mL of *E. coli* ER2738 culture (OD$_{600}$ = 0.1) in LB medium with 50 μg/mL tetracycline. The culture was incubated at 37 °C for 4 h with shaking at 120 rpm. Afterwards, the culture was centrifuged at 5000 rpm for 1 hour at 4 °C. The pellet was resuspended in 1 mL of resuspension buffer (25 mM HEPES, pH 7.4) and centrifuged at 10,000 rpm for 5 min at 4 °C. The solution was then mixed with 200 μL of 20 % (w/v) PEG-8000, 2.5 M NaCl and incubated on ice for 1 hour, followed by a final centrifugation at 10,000 rpm for 45 min at 4 °C. The phage pellet was resuspended in 100 μL of resuspension buffer, and the concentration was measured at 269 nm. The phage solution was stored at 4 °C.

2.2.2. Plasmid isolation and sequencing

To isolate plasmid DNA, 10 μL of the phage solution was mixed with 90 μL of TBS buffer and 200 μL of a 20 % (w/v) PEG-8000, 2.5 M NaCl solution and incubated at RT for 20 min. The mixture was centrifuged at 14,000 rpm for 10 min at 4 °C, and the pellet was resuspended in 200 μL of Na-acetate: TE buffer (10:1). DNA was precipitated by adding 500 μL of 99 % ethanol, incubated for 15 min, and centrifuged at 14,000 rpm for 10 min at 4 °C. The pellet was washed with 250 µL of 70 % ethanol, dried at 30 °C for 7 min, resuspended in 40 µL of ddH₂O, and the concentration was measured. DNA was amplified by PCR, sequenced at Heinrich Heine University Düsseldorf, and analyzed using the TSAT program (developed at IBI7 Institute at Research Center Jülich) (Altendorf et al., 2024) Sequences were ranked by enrichment and empty scores (Sevenich et al., 2022).

2.3. Peptides

All peptides were purchased from GenScript Biotech (Rijswijk, Netherlands) BV as lyophilized powder with >90 % purity. All peptides are all in the L-configuration and consist of 16 amino acids, except for P4, which contains 14 amino acids. All peptides are amidated at their C-terminus and acetylated at the N-terminus. Based on the P1 sequence, three scrambled peptides with randomly changed sequence were generated. The purity of each peptide was verified by an analysis certificate from GenScript Biotech (Rijswijk, Netherlands) BV (Supplementary Figs. S2-S4 and Table S1). The peptides were analyzed using high-performance liquid chromatography (HPLC) with an Inertsil ODS-3 column (4.6 × 250 mm). Mass spectrometry analysis was conducted using the Electrospray Ionization (ESI) technique.

2.4. Inhibition assay

An inhibition assay was performed using a fluorescence resonance energy transfer (FRET)-based assay with the synthesized fluorogenic substrate DABCYL-Arg-Ala-Gly-Gly-↓Tyr-Ile-Phe-Ser-EDANS (BACHEM, Bubendorf, Switzerland) (Eberle et al., 2021; Hu et al., 2016), which mimics the natural substrate sequence between the nsPs in the viral polyprotein. The assay was conducted in 96-well plates with a reaction solution of 20 mM Bis-Tris-Propane buffer at pH 7.5. The final reaction volume in each well was 100 µL, containing 10 µM nsP2^{pro} and 9 µM substrate. The peptides were dissolved in 100 % dimethyl sulfoxide (DMSO) to a final stock concentration of 10 mM. A DMSO control with concentrations ranging from 0 % to 1 % was included to assess any potential effects of this substance on protease activity (Supplementary Fig. S5). The final concentration of the peptides in the reaction mixture was 50 µM. The Fluorescence intensities (excitation at 340 nm and emission at 490 nm) were measured at 30-second intervals over a 30-minute period at 37 °C using a CLARIOstar plate reader (BMGlabtech, Ortenberg, Germany) and the protease activity and inhibition were calculated using equation 1 (Eberle et al., 2021):

$$\textit{Protease activity}\,\% = \frac{\textit{Intensity of enzymatic activity after inhibiton}}{\textit{Intensity of enzymatic activity}} \times 100$$

To investigate the specificity of the identified peptides, a scrambled version of the P1 peptide, designated as SP1-SP3, was included in the assay at the same concentration as the experimental peptides. This control peptide served to evaluate any potential nonspecific binding or inhibition. All measurements were performed in triplicate, and data are presented as mean ± SD.

2.5. Determination of half maximal inhibitory concentration (IC_{50})

The protease was used at a concentration of 10 µM, while the substrate concentration was maintained at 9 µM. The inhibitory effects of the peptides at various concentrations (0–900 µM) were measured using excitation at 340 nm and emission at 490 nm. To minimize peptide aggregation, the buffer composition, experimental temperature, and duration of the experiment were optimized individually for each peptide (Table 2).

Table 2
Conditions for determination of the IC_{50} values of peptides against CHIKV nsP2^{pro}.

Peptides	Temp. [°C]	Cycle [sec]	Time [min]	Buffer
P1	37	30	10	20 mM Bis-Tris-Propane, pH 7.5, 0.1 Triton-X 100
P2, P4, P5	20	30	20	20 mM Bis-Tris-Propane, pH 7.5,

All measurements were performed in triplicate and data are presented as mean ± SD.

2.6. Determination of the inhibition mode of the peptide inhibitor

The mode of inhibition was investigated using the (FRET)-based assay described before. To evaluate the mode of inhibition of peptide P1, the enzymatic activity of nsP2^{pro} was measured at varying concentrations of both the inhibitor and the substrate in 20 mM Bis-Tris-Propane pH 7.5, while maintaining a constant protease concentration of 10 µM (Table 3).

2.7. CD spectroscopy

Peptides were prepared in ddH₂O containing 5 % DMSO at a final concentration of 500 µM for secondary structure analysis. The spectra were recorded at 18 °C using a 0.1 mm pathlength cuvette across a wavelength range of 190–250 nm with a Jasco J-1100 spectropolarimeter (Jasco GmbH, Pfungstadt, Germany). Additionally, CD spectroscopy was performed to evaluate the folding quality of the purified nsP2^{pro} after the purification process. The protease was diluted in 10 mM sodium phosphate buffer (2.39 mM NaH_2PO_4, 7.6 mM Na_2HPO_4, pH 7.5) to a final concentration of 5 µM, and measurements were conducted seven times using a 1 cm pathlength cuvette at 18 °C, covering a wavelength range of 190–260 nm (Supplementary Fig. S1). The baseline spectrum averaged from multiple measurements, was subtracted from the corresponding averaged sample spectrum to obtain corrected data. The results were expressed as molar ellipticity ([θ]) and calculated using the following equation 2:

$$[\theta]\lambda \ = \frac{\theta}{(c * l * n)}$$

Where θ is the ellipticity measured at the wavelength λ (deg), c is the protein concentration (mol/L), l is the cell path length (cm), and n is the number of amino acids. The secondary structure content was determined from CD results, and the K2D3 online tool (https://cbdm-01.zdv.uni-mainz.de/~andrade/k2d3/) was utilized to predict the secondary structure composition.

2.8. Secondary structure prediction of the selected peptides

The I-TASSER tool (https://zhanggroup.org/I-TASSER/) was used to predict the secondary structure of the selected peptides (P1-P6). Model confidence is evaluated using the C-score, which typically ranges from −5 to 2 with higher values indicating more reliable predictions. Additionally, I-TASSER calculates a TM-score (between 0 and 1) to measure the alignment quality between structural models. Higher TM-scores indicate greater structural agreement (Yang et al., 2015).

Table 3
Applied concentration of substrate and peptides in the inhibition mode assay.

Substrate conc. [µM]	0	3	6	9	12	15
Inhibitor conc. [µM]	0 0.75 1.5 3	0 0.75 1.5 3	0 0.75 1.5 3	0 0.75 1.5 3	0 0.75 1.5 3	0 0.75 1.5 3

2.9. Equilibrium dissociation constant determination using microscale thermophoresis (MST)

To determine the equilibrium dissociation constant (K_D), an MST (microscale thermophoresis) assay was conducted. The peptide was first labeled with CF™633 succinimidyl ester dye (Sigma-Aldrich, St. Louis, MO, USA). A total of 1 μmol of dye was warmed to room temperature and dissolved in DMSO to prepare a 10 mM stock solution. The peptide was diluted in 1 M sodium bicarbonate buffer (pH 8.3) to a final concentration of 0.12 mM in a volume of 50 μL. Following this, 50 μL of the dye solution was added to the peptide solution, and the mixture was incubated in the dark for one hour. Subsequently, the labeled peptide was purified using reversed-phase high-performance liquid chromatography (RP-HPLC) on an Agilent 1260 Infinity II system (Agilent Technologies, Santa Clara, CA, USA). A volume of 20 μL of the labeled peptide solution was injected into a Zorbax 300SB-C8 column (Agilent Technologies, Santa Clara, CA, USA) at 25 °C. The mobile phase consisted of buffer A (0.1 % trifluoroacetic acid, TFA) and buffer B (acetonitrile with 0.1 % TFA). The peptide was eluted using a linear gradient of 10 to 80 % of buffer B over 40 min. Chromatograms were recorded at three wavelengths: 214 nm, 280 nm, and 633 nm (Supplementary Fig. S6). Collected fractions were frozen using liquid nitrogen and lyophilized overnight. The lyophilized sample was reconstituted in 50 μL of 20 mM Bis-Tris-Propane buffer (pH 7.5). Absorbance measurements were taken at 280 nm and 630 nm using a UV–Vis spectrophotometer. The concentration of the labeled peptide was then calculated using the following equation 3:

$$labeled\ peptide\ mg\Big/ml = \frac{(A280 - (AMax * CF))}{E} * df$$

The A280 and AMax represent the absorbance readings of the labeled peptide at 280 nm and the absorption maximum, respectively, while CF refers to the absorbance correction factor (0.48 for the CF™633 dye), and E is the extinction coefficient of the peptide. df indicates the dilution factor. The labeling process was carried out following the guidelines provided in the Sigma-Aldrich (St. Louis, MO, USA) technical bulletin. The equations were adapted to calculate the concentration of the labeled peptide. The labeling efficiency was determined separately and calculated to be approximately 54 %. To prepare the samples for the MST assay, a labeled peptide stock solution with a concentration of 2 μM was prepared. A 16-step, 1:2 serial dilution series of unlabeled CHIKV nsP2^{pro} was created. Subsequently, 10 μL of the labeled peptide solution was added to each diluted protease solution, resulting in a final concentration of 1 μM and protease concentrations ranging from 2 nM to 74 μM. The samples were loaded into Monolith series premium capillaries (NanoTemper Technologies GmbH, Munich, Germany) and measured at 37 °C with 100 % LED power and 100 % MST power. The results were analyzed using the software provided by NanoTemper Technologies (Munich, Germany). To determine the best fit for calculating the equilibrium dissociation constant (K_D), the K_D model, based on the mass-action kinetics model, was used in the software. The program provided the fraction bound for each dose, and the K_D was determined by fitting the data to this model. Measurements were performed in triplicate, and the mean fraction bound per dose was calculated and analyzed using Prism software. The final K_D value was reported as the mean of the individual K_D values calculated for each measurement by the software.

2.10. Cell viability assay

Cell viability assay was performed using Vero cells, which are kidney epithelial cells derived from the African green monkey (*Chlorocebus aethiops*) and were generously provided by the group of Dr. Lisa Müller located at the Virology Institute, University Hospital Düsseldorf. The cells were cultured under standard conditions in a humidified incubator at 37 °C with 5 % CO_2. Peptide cytotoxicity was assessed by exposing cells to varying concentrations of peptides (dissolved in either water or DMSO and diluted in DMEM medium) ranging from 0 to 100 μM. The concentrations were selected based on the determined P1 IC_{50} value (4.7 μM). To assess the potential cytotoxic effects at different concentrations, peptide concentrations ranging from sub-IC_{50} values up to 100 μM were tested. The upper concentration limit (100 μM) was chosen to provide a broad evaluation of the peptide's effects on cell viability. This range allowed us to observe any potential cytotoxicity and to demonstrate the peptide's toxicity at higher concentrations. As a negative control, 0.1 % Triton X-100 was added to five wells to induce complete cell lysis. The plates were then incubated overnight under identical conditions to allow cytotoxic effects to develop. The following day, 10 μL of MTT labeling reagent from the Cell Viability Kit (Roche Diagnostics GmbH, Mannheim, Germany) was added to each well. Metabolically active cells converted MTT into formazan crystals, providing a measure of cell viability. After 4 h of incubation, 100 μL of solubilization buffer (Solution No. 2) was added to dissolve the crystals and the plates were incubated overnight to ensure complete solubilization. Absorbance was measured at 570 nm (signal) and 660 nm (reference) using a CLARIOstar plate reader (BMGlabtech, Ortenberg, Germany). The Cell viability percentages were calculated using the following formula equation 4:

$$\frac{(A570 - A660)of\ treated\ cells}{(A570 - A660)of\ control\ (not\ treated\ cells)} \times 100$$

2.11. Molecular docking

To predict the binding mode of peptide P1 to CHIKV nsP2^{pro}, we conducted protein-peptide blind docking at the web servers of three different docking programs: ClusPro (Jones et al., 2022), HDock (Yan et al., 2020) and Galaxy Tongdock (Park et al., 2019). The structure of CHIKV nsP2^{pro} used for docking was obtained through clustering analysis of a concatenated 20 μs of the protein, as explained hereinafter. The peptide structure was modeled using the I-TASSER tool (Zhou et al., 2022). The top-ranked poses obtained with each docking program were subjected to subsequent analyses to assess the most likely binding mode.

2.12. Molecular dynamics simulations

The structure of CHIKV nsP2^{pro} was retrieved from the PDB 3TRK. Protonation states of ionizable residues at pH 7.4 were predicted using propKa at the PDB2PQR web server (Dolinsky et al., 2004). The protein was then embedded in an octahedral box with edges spanning at least 10 Å from the solute surface. The box was filled with OPC water molecules (Izadi et al., 2014) and counterions to neutralize the protein net charge. The force field ff19SB (Tian et al., 2020) was employed to assign parameters for the protein atoms (Case et al., 2005)

The system was subjected to energy minimization (EM) to resolve steric clashes before advancing to the equilibration steps. A total of 5000 EM cycles were performed, with the first 3000 cycles using the steepest descent algorithm and the remaining 2000 cycles employing the conjugate gradient algorithm. Heating was subsequently carried out by linearly increasing the system's temperature from 10 K to 310 K under constant volume conditions over 500 ps. Initial atomic velocities were assigned from a Maxwell-Boltzmann distribution at 10 K. Following the heating phase, the pressure was equilibrated at 1 bar over an additional 500 ps while maintaining the temperature at 310 K. During both equilibration steps, harmonic position restraints ($k = 10\ kcal \cdot Å^{-2} \cdot mol^{-1}$) were applied to the protein's heavy atoms. The harmonic restraints were gradually removed in $2\ kcal \cdot Å^{-2} \cdot mol^{-1}$ strides during four consecutive 1 ns MD simulations conducted in the NPT ensemble. The temperature and pressure during equilibration were controlled using the Berendsen thermostat and barostat, respectively. A timestep of 2 fs was used to integrate the equations of motion in all these steps, employing the leapfrog algorithm (Case et al., 2005). A 2 μs productive MD simulation was subsequently performed in the NVT ensemble at 310 K, with frames saved every 60,000 steps. The temperature during the removal of harmonic restraints and the productive simulations was controlled using the Langevin thermostat (Case et al., 2005). Hydrogen mass repartitioning was applied to increase the integration timestep to 4 fs during the 2 μs simulation (Hopkins et al., 2015). A cutoff of 10 Å was used for short-range interactions, while long-range electrostatic interactions were calculated with the Particle Mesh Ewald (PME) method. To enhance conformational sampling, 10 replicate MD simulations were performed by varying the initial random velocities assigned to atoms during the heating phase (Case et al., 2005).

A similar protocol was employed for the MD simulations carried out for CHIKV nsP2^{pro} in complex with peptide P1. The ACE and NME caps were added to the N- and C-termini of the peptide, respectively, and parameters for its atoms were derived for the ff19SB force field. 1 μs productive runs were conducted for the three top-ranked poses bound to the protease. Moreover, an extension of 2 μs was performed for the complex showing the largest affinity. No replicate MD simulations for the protein-peptide systems were conducted.

2.13. MM-GBSA free energy calculations

Molecular Mechanics Generalized-Born Surface Area (MM-GBSA) free energy calculations were carried out for the three top-ranked poses of peptide P1 in complex with CHIKV nsP2^{pro} using the program MMPBSA.py (Miller et al., 2012) of Amber22 (Case et al., 2005). The single trajectory approach, where frames from the free protein and the free ligand are extracted from the trajectory of the complex, was followed. Calculations were performed with 542 frames evenly collected from the last 0.5 μs of each analyzed trajectory. The GB-neck2 (igb = 8) implicit solvation model (Nguyen et al., 2013) was employed to estimate the polar solvation energy. Dielectric constants of 1 and 80 were assigned for the internal space of the solute and for the solvent, respectively, and a salt concentration of 0.1 M was set. A surface tension coefficient of 0.0072 kcal·Å^{-2}·mol^{-1} was used for the calculation of the surface free energy component (Case et al., 2005). Since the configurational entropy was neglected, the predicted free energies are referred to as effective binding free energies (ΔG_{eff}). To evaluate the contribution of interface residues to the binding free energy, the protocol of per-residue free energy decomposition implemented in MMPBSA.py was employed. This calculation was performed using the same implicit solvation model and conditions stated in the previous paragraph.

2.14. Trajectory analyses

Root-mean-square-deviations (RMSDs) and interatomic distances during the MD simulations were calculated with the *rmsd* and *distance* commands of *cpptraj* of Amber22. For trajectory clustering, the command *cluster* of the same program was employed. The RMSD of CHIKV nsP2^{pro} active site residues were set as a metric for clustering with the hierarchical agglomerative algorithm (Case et al., 2005). As a rule of thumb, five clusters were generated for each analyzed trajectory.

2.15. Statistical analysis

Statistical analysis, including the calculation of confidence intervals and significance levels (p-values), was performed using GraphPad Prism. Descriptive statistics were used to calculate confidence intervals, and one-way ANOVA followed by Tukey's post hoc test was conducted to assess differences between groups. Statistical significance was determined at $p < 0.05$ (*), $p < 0.01$ (**), and $p < 0.001$ (***).

3. Result

3.1. Phage display peptide selection

Phage display technology was utilized to identify specific peptide binders targeting the CHIKV nsP2^{pro} (Fig. 1). The selection process involved three rounds of phage display to isolate peptides with high affinity and specificity for the target protein. Subsequently, DNA was extracted from the phage and sequenced using next-generation sequencing (NGS). The NGS data were analyzed using the TSAT program (Altendorf et al., 2024), which ranked the sequences based on two metrics: the empty score and the enrichment score. Peptides with higher empty and enrichment scores were considered to have greater specificity for CHIKV nsP2^{pro}. Based on these criteria, six peptides were selected and named as P1, P2, P3, P4, P5, and P6 (Table 4).

3.2. Primary inhibition test of selected phage display peptides

A primary inhibition test, based on a FRET-based assay (Eberle et al., 2021; Hu et al., 2016) was conducted to evaluate the peptides' inhibitory potential on protease activity. The assay utilized peptides at a concentration of 50 μM, which were added to the nsP2^{pro}. Fluorescent intensity was recorded at 30-second intervals over 30 min at 37 °C. The results revealed that four out of the six peptides (P1, P2, P4 and P5) significantly inhibited the protease activity (Fig. 2A). Peptides P1 and P2 demonstrated the strongest inhibition, reducing protease activity by over 50 %, while peptides P4 and P5 exhibited moderate inhibition, reducing activity by approximately 50 %. In contrast, peptide P3 showed no detectable inhibitory effect, whereas peptide P6 reduced protease activity by approximately 30 %. A control experiment with three scrambled peptides (Sequence based on P1, Table S1) showed no significant effect on the nsP2^{pro} activity (Fig. 2B).

3.3. Determination of the half maximal inhibitory concentration (IC_{50}) of selected peptides

Based on the results of the primary test, the peptides with the strongest inhibition effect against CHIKV nsP2^{pro} (P1, P2, P4 and P5) were further investigated to evaluate their efficacy. The assay was performed as described before, with peptide concentrations ranging from 0 to 900 μM and 10 μM of nsP2^{pro}. Changes in the fluorescence intensity was recorded at 37 °C in 30-s intervals for 30 min. However, peptide aggregation occurred within 3–5 min, preventing accurate IC_{50} determination under these conditions. To address this issue, assay conditions were optimized to reduce peptide aggregation and extend measurement duration (Table 2). Fig. 3 illustrates IC_{50} of the peptides. Peptide P1 showed the strongest inhibition, with an IC_{50} value of 4.6 μM (Fig. 3A). Peptides P2 and P5 exhibited IC_{50} values of 194.7 μM (Fig. 3B) and 316.9 μM (Fig. 3C). Peptide P1 achieved complete inhibition of nsP2^{pro} activity at approximately 175 μM, while peptides P2 and P5 required up to 900 μM for significant inhibition (Supplementary Fig. S7).

3.4. Determination of the P1 inhibition mode

The IC_{50} results identified peptide P1 as the most potent inhibitor of CHIKV nsP2^{pro}, with an IC_{50} value of 4.6 μM. Based on this finding, P1 was selected for further investigation, including determination of its mode of inhibition. An FRET-based assay was performed by varying the concentrations of both the peptide (P1) and the substrate. The analysis revealed that increasing the concentration of P1 reduced substrate affinity, as indicated by an increase in the K_m constant. The data were subsequently analyzed using a Lineweaver-Burk plot. (Fig. 4A).

3.5. Determination of the equilibrium dissociation constant using microscale thermophoresis (MST)

Microscale thermophoresis (MST) measurements were used to determine the equilibrium dissociation constant (K_D) by analysing changes in molecular movement induced by a temperature gradient generated with an infrared laser. The peptide, labeled with CF™633 dye, was added to a series of dilutions of the protease ranging from 2 nM

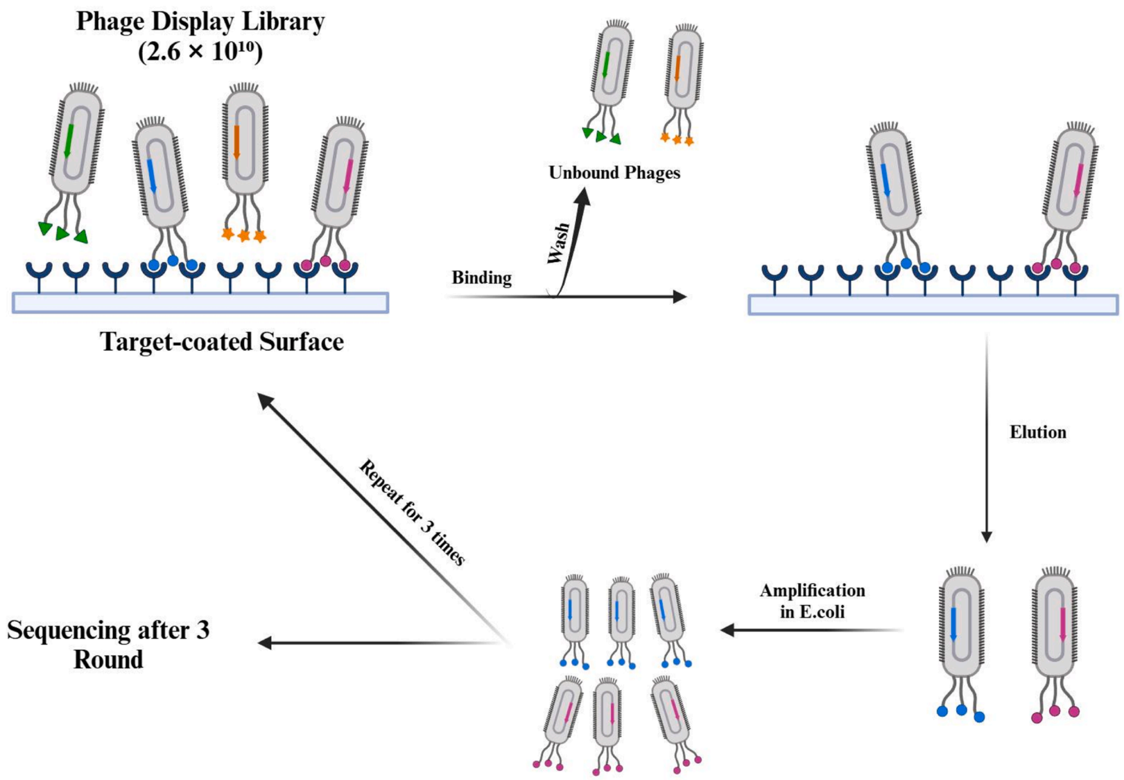

Fig. 1. Schematic representation of phage display technique and workflow. Modified figure from Eberle et al., 2023.

Table 4
Selected peptides from phage display.

Peptides	Sequence	Empty score	Enrichment score
P1	VMPWDEWLTKRKPELP	221	91
P2	HTSRIYIPSPIHAENI	61	38
P3	MEASGVNYQNMNKQTT	54	34
P4	FTMSPPLQMPSKNY	231	287
P5	NAMSHVMEGSHINWDA	220	136
P6	YISPQYYGETWVTTIG	167	104

to 74 μM. The motion of the peptide and protease complex was recorded at 37 °C with 100 % MST and LED power. The experiment was performed in triplicate. Based on the quantified data and analysis, a fraction-bound versus dose graph (Fig. 4B) was generated, yielding a K_D value of 1.39 ± 0.61 μM for peptide P1.

3.6. *Cytotoxicity effects of peptide P1 on Vero cells*

To assess the toxicity of peptide P1, Vero cells were used. These cells are a standard cell line widely employed in CHIKV infection research and other alphavirus studies due to their permissivity to these viruses (Ribeiro et al., 2018). To evaluate the toxicity of P1, Vero cells were exposed to varying concentrations of the peptide (0–100 μM), and cytotoxicity was assessed using the MTT assay. The results showed that peptide P1 dissolved in water exhibited low toxicity, with approximately 83 % cell viability observed at a concentration of 100 μM. In contrast,

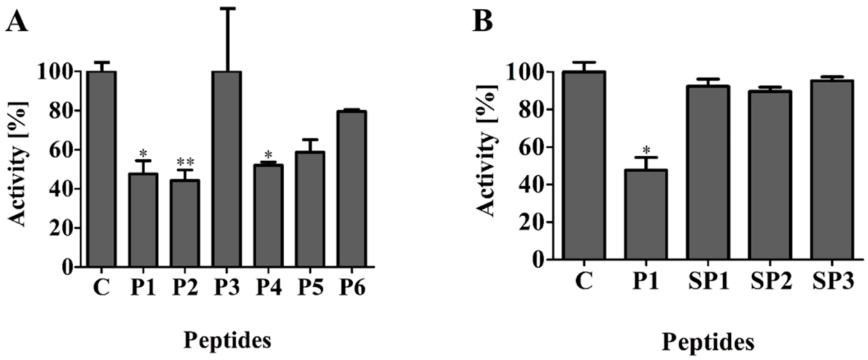

Fig. 2. Inhibition analysis of selected peptides (P1–P6) and scrambled peptide controls against CHIKV nsP2^{pro} activity. The inhibition analysis of CHIKV nsP2^{pro} by six identified peptides (P1–P6) and the specificity assessment of P1using scrambled peptides (SP1–SP3). **(A)** Primary inhibition assay, CHIKV nsP2^{pro} was tested at a 10 μM concentration, while peptides (P1–P6) were applied at 50 μM. The control (C) represents protease activity in the absence of peptides. **(B)** Specificity assessment of P1, The inhibitory activity of P1 was compared to three scrambled peptides (SP1–SP3) under the same conditions (10 μM protease, 50 μM peptides) to evaluate potential nonspecific inhibition effects. Statistical significance was determined using one-way ANOVA, followed by Tukey's test. Asterisks indicate significant differences from the control ((A): 0 μM inhibitor and (B): P1). Asterisks denote statistically significant differences from the control group as determined by one-way ANOVA and Tukey's test, where $p < 0.05$ (*), $p < 0.01$ (**). Data are presented as mean ± SD from three independent experiments ($n = 3$).

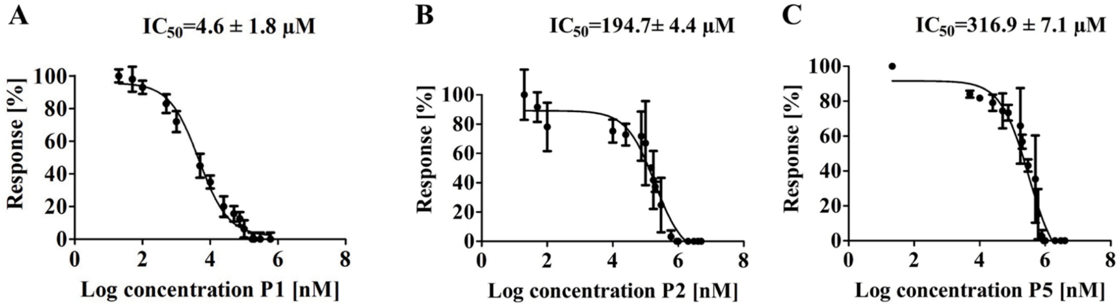

Fig. 3. Half maximal inhibitory concentration (IC_{50}) values, determined for the peptides P1, P2, and P5. Panels **A-C** present the dose-response curves for peptides (P1, P2, and P5) against CHIKV $nsP2^{pro}$.

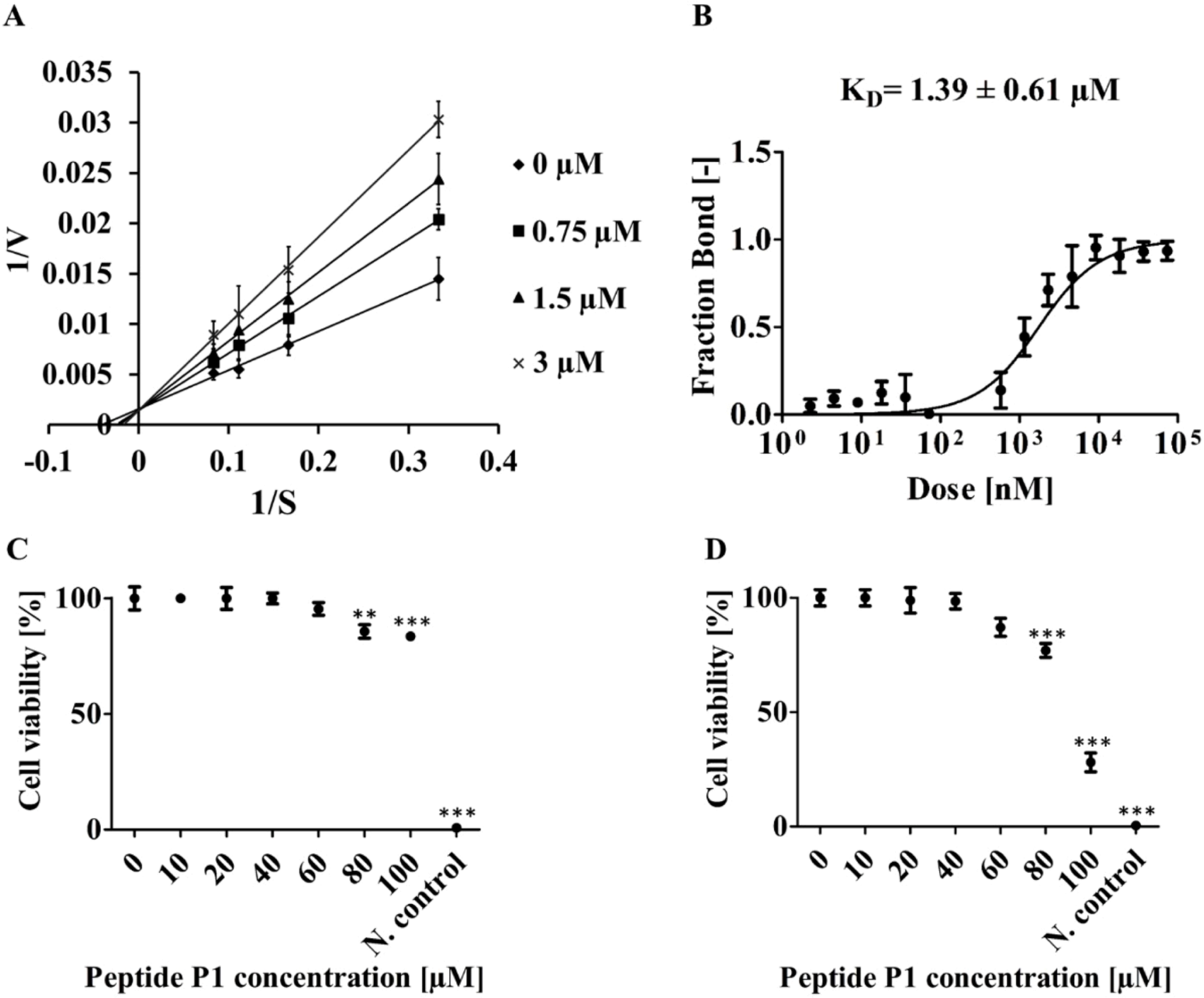

Fig. 4. Inhibition, binding, and toxicity assessment of peptide P1 against CHIKV $nsP2^{pro}$ (A) The inhibition mode of peptide P1 was determined using a Lineweaver-Burk plot. The intersection on the y-axis, characteristic of competitive inhibitors, indicates that peptide P1 acts as a competitive inhibitor. This suggests that peptide P1 competes with the substrate for binding to the enzyme's active site. As a result, the enzyme's affinity for the substrate decreases, leading to an increase in K_m. **(B)** Microscale thermophoresis (MST) assay demonstrating the binding affinity of peptide P1 to the CHIKV $nsP2^{pro}$, with a equilibrium dissociation constant (K_D) of 1.39 ± 0.61 μM. **(C)** MTT assay of peptide P1 dissolved in water, tested against Vero cells at concentrations ranging from 0 to 100 μM. The negative control used was 0.1 % Triton X-100. **(D)** MTT assay of peptide P1 dissolved in DMSO, tested against Vero cells at concentrations ranging from 0 to 100 μM. The negative control used was 0.1 % Triton X-100. Data from MTT assays are presented with 95 % confidence intervals for each group (see Supplementary Table S2). Significant differences between groups were determined by single-factor ANOVA. Asterisks indicate statistical significance, determined using one-way ANOVA, followed by Tukey's test. Asterisks indicate significant differences from the control (0 μM inhibitor). Asterisks denote statistically significant differences from the control group as determined by one-way ANOVA and Tukey's test, where $p < 0.01$ (**) and $p < 0.001$ (***).

when peptide P1 was dissolved in DMSO, cell viability was approximately 77 % at 80 μM but decreased significantly to 28 % at 100 μM (Fig. 4C,D).

3.7. Secondary structure prediction of the selected peptides

The peptide structure was predicted using the I-TASSER tool with each model assigned a confidence score (C-score) of [−5,2], indicating the reliability of the predictions. To validate these models, the secondary structure content, specifically the proportions of alpha-helices and beta-sheets, was experimentally determined through circular dichroism (CD) spectroscopy (Supplementary Table S3). The CD spectroscopy data were then compared to the predicted structures. Table S3 illustrates the predicted peptide structures alongside their corresponding CD spectroscopy analyses. These structures represent potential conformations within a structural ensemble in solution. The comparison between experimental and predicted data (Supplementary Table S3 and Fig. S8) demonstrated that most peptides exhibit a combination of random coil and alpha-helical structures, except for peptides P2, P4, and P6. Furthermore, the I-TASSER predictions aligned well with the secondary structure data obtained from CD spectroscopy.

3.8. Structural analysis and molecular modeling

MD simulations were performed to explore the dynamic properties of CHIKV nsP2^{pro}. Fig. 5A illustrates the flexibility of the protease's active site over a 20 μs timescale. Due to interdomain motion, a flap formed by residues A1080 to H1083 can adopt positions either close to or far from the C-terminal domain, leading to closed and open conformations of the active site, respectively. Interestingly, the crystal structure of CHIKV nsP2^{pro} (PDB 3TRK) exhibits a closed active site, which is not suitable for investigating the binding of orthosteric ligands. By measuring the distance between the flap and residue M1242 in the opposing domain, and defining a threshold of 19 Å based on visual inspection, we observed that the active site remains in a closed state approximately 87 % of the time, transitioning to an open state 13 % of the time (histogram in Fig. 5A).

Through clustering analysis, we identified five representative structures possessing distinct orientations of the catalytic domain relative to the C-terminal domain (Fig. 5B). As shown in the figure, the active site adopts a more open conformation as the flap moves farther away from a highlighted loop on the C-terminal domain (residues 1202–1206). Among the four central structures with open active sites, we selected the one closest (beige) to the central structure of the closed state (green) for subsequent peptide binding studies (Fig. 5B). This selection seeks to minimize the risk of the open conformation being a result of force-field artifacts, while ensuring the peptide can bind effectively within the open active site (the open cavity illustrated in Fig. 5C).

Subsequently, blind docking was performed using three different programs: ClusPro (Jones et al., 2022), HDock (Yan et al., 2020) and Galaxy Tongdock (Park et al., 2019) to predict the binding mode of peptide P1 to CHIKV nsP2^{pro}. The starting conformations of the peptide and the target protease employed for the docking studies are those depicted in supplementary Fig. 8A and Fig. 5C, respectively. Remarkably, P1 conformations interacting with the protein active site were consistently predicted as top-ranked solutions by all the three docking programs (Fig. 6A–C), in agreement with the experimental results. Each of the top-ranked docking poses was subjected to a 1 μs MD simulation to evaluate the stability of the predicted complex. The RMSD plots in Fig. 6D–F reveal that the peptides underwent moderate (<10 Å for Hdock and Galaxy Tondock poses) to significant (>10 Å for the ClusPro pose) changes in binding mode relative to the docking poses during the simulations. Despite these initial changes, relatively stable binding conformations were consistently observed throughout the second half of each trajectory.

The most favorable binding mode of P1 to CHIKV nsP2^{pro} was identified through MM-GBSA free energy calculations. Frames from the three MD trajectories, excluding the first 0.5 μs used for equilibration, were analyzed for this purpose. The resulting ΔG_{eff} values for the final segment of the analyzed MD simulations are summarized in Table S4. The binding mode sampled during the final segment of the MD simulation initiated from the Hdock docking pose exhibited the most negative ΔG_{eff} value (−62.56 kcal/mol), significantly outperforming the other two. Extending the MD simulation of the Hdock pose to 2.5 μs reinforced its stability. In fact, the ΔG_{eff} value calculated for the last 0.5 μs of the extended trajectory closely matched that of the 1 μs MD simulation (Supplementary Table S4). Additionally, the peptide RMSD plot for the extended trajectory (Supplementary Fig. S9) indicated no major conformational changes. Overall, the previous analyses suggest that the conformations sampled during the last 2 μs of the Hdock pose simulation are likely to be representative of the native binding mode of P1 at the CHIKV nsP2^{pro} active site.

Central structures for the 2.5 μs MD simulation of the CHIKV nsP2^{pro}:P1 complex were finally obtained through clustering analysis. The interface of the central structure from the largest cluster is shown in Fig. 7A. As observed, the peptide extends along the open active site, with most of its aromatic and hydrophobic residues buried at the interface, significantly contributing to binding. This is supported by the substantial free energy contributions (ΔG_{res}) of residues M2, W4, and W7 (Fig. 7B). Similarly, CHIKV nsP2^{pro} residues interacting with the peptide's key hotspots also display notable ΔG_{res} values, such as N1011, A1046, Y1079, L1205, M1238, and M1242 (Fig. 7B). These interactions contribute to the negative nonpolar free energy component, ultimately resulting in the favorable ΔG_{eff} value observed for the CHIKV nsP2^{pro}:P1 complex (Supplementary Table S4). Conversely, polar residues at the interface generally exhibited small energy contributions to complex formation, except for K10 and R11, which possess significantly favorable ΔG_{res} values (Fig. 7B). However, these polar residues compensate for the loss of favorable interactions with water upon binding by forming intermolecular hydrogen bonds (H-bonds), as depicted in Fig. 7A.

4. Discussion

Chikungunya virus (CHIKV) is an emerging virus with infections rising rapidly due to the global spread of its vector, posing a significant public health challenge. While several lead compounds such as 1,3-Thiazolbenzamide derivatives, Hesperetin (HST) have been identified as inhibitors of the CHIKV nsP2^{pro}, none has yet been approved as therapeutic agents for Chikungunya fever (Eberle et al., 2021; Ivanova et al., 2021). In this study, six different peptides were identified using phage display as specific binders against the nsP2^{pro} (Table 4). Among these, four peptides (P1, P2, P4, and P5) exhibited inhibitory effects on the protease in a primary inhibition test, with inhibition rates of ≤50 % (Fig. 2). The IC_{50} value of peptide P1 for the nsP2^{pro} was determined to be 4.6 μM (Fig. 3A), making it the most potent inhibitor identified in this study. Peptides P2 and P5 had IC_{50} values of 194.7 μM and 316.9 μM, respectively (Fig. 3B,C). However, the IC_{50} value of peptide P4 could not be determined due to aggregation occurring within 2–4 min under the assay conditions. These results highlight peptide P1 as the strongest inhibitor. The scrambled P1 peptides (SP1-SP3) (Supplementary Table S1 and Fig. 2B) showed a weak effect against the CHIKV nsP2^{pro} activity at the tested concentration of 50 μM. These results indicates that the inhibitory activity of P1 is sequence-dependent and highly specific. The inhibition mode assay revealed that peptide P1 increases the Michaelis-Menten constant (K_m), while the maximum velocity (V_{max}) remains unchanged (Fig. 4A) and this indicates a reduced affinity of the enzyme for its substrate, which is characteristic for a competitive inhibitor (Blat, 2010). Affinity measurements using MST (Jerabek-Willemsen et al., 2014) showed that peptide P1 has an equilibrium dissociation constant (K_D) of approximately 1.39 μM (Fig. 4B), demonstrating a binding affinity to its target in the low μM range. A comparison of P1 revealed a lower IC_{50} compared to other identified small molecules from various studies, such as the 1,3-thiazolbenzamide

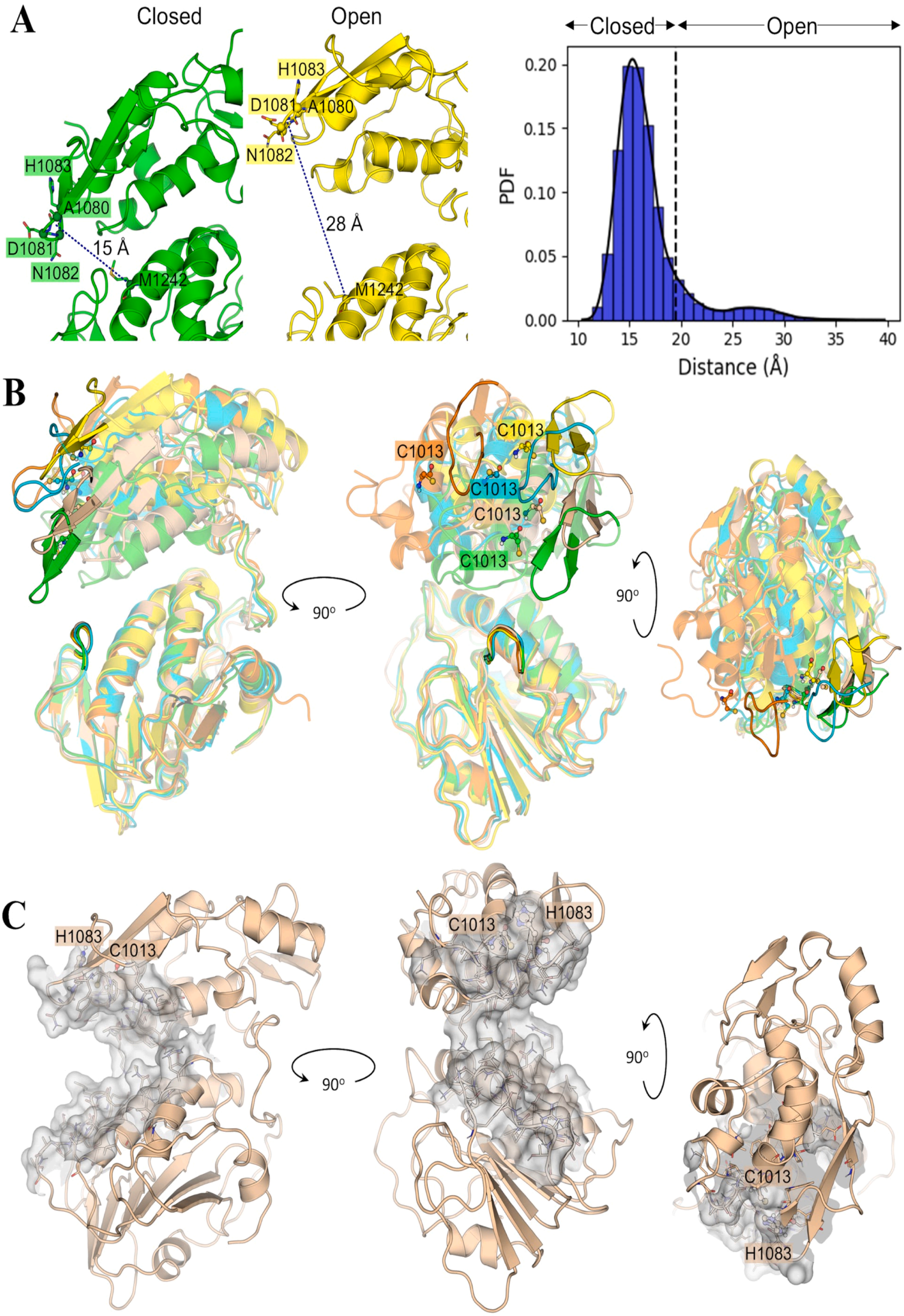

(caption on next page)

Fig. 5. Conformational dynamics of CHIKV nsP2^{pro}. (A) Structural representations of two snapshots of CHIKV nsP2^{pro}, illustrating closed and open conformations of the active site resulting from interdomain motion. To monitor these conformational changes throughout the MD simulations, the distance between the Cα atoms of residues A1080, D1081, N1082, and H1083 on the flap and the Cα of M1242 on a neighboring α-helix in the opposite domain was measured. The graph on the right shows the distribution of these distances along the 20 μs concatenated MD trajectory, with the dashed line indicating the threshold used to define open and closed states. **(B)** Structural representation of five central structures derived from clustering the 20 μs concatenated trajectory. The C-terminal domains (lower domain) were aligned to highlight the motion of the N-terminal catalytic domain (upper domain). The catalytic Cys residue (C1013) is depicted as spheres and sticks. Additionally, the flap of the catalytic domain and a loop interacting with it in the closed conformation are highlighted. **(C)** Surface representation of the open conformation of the active site, highlighting the catalytic residues C1013 and H1083. This snapshot was selected for the prediction of the CHIKV nsP2^{pro}: peptide complex structure.

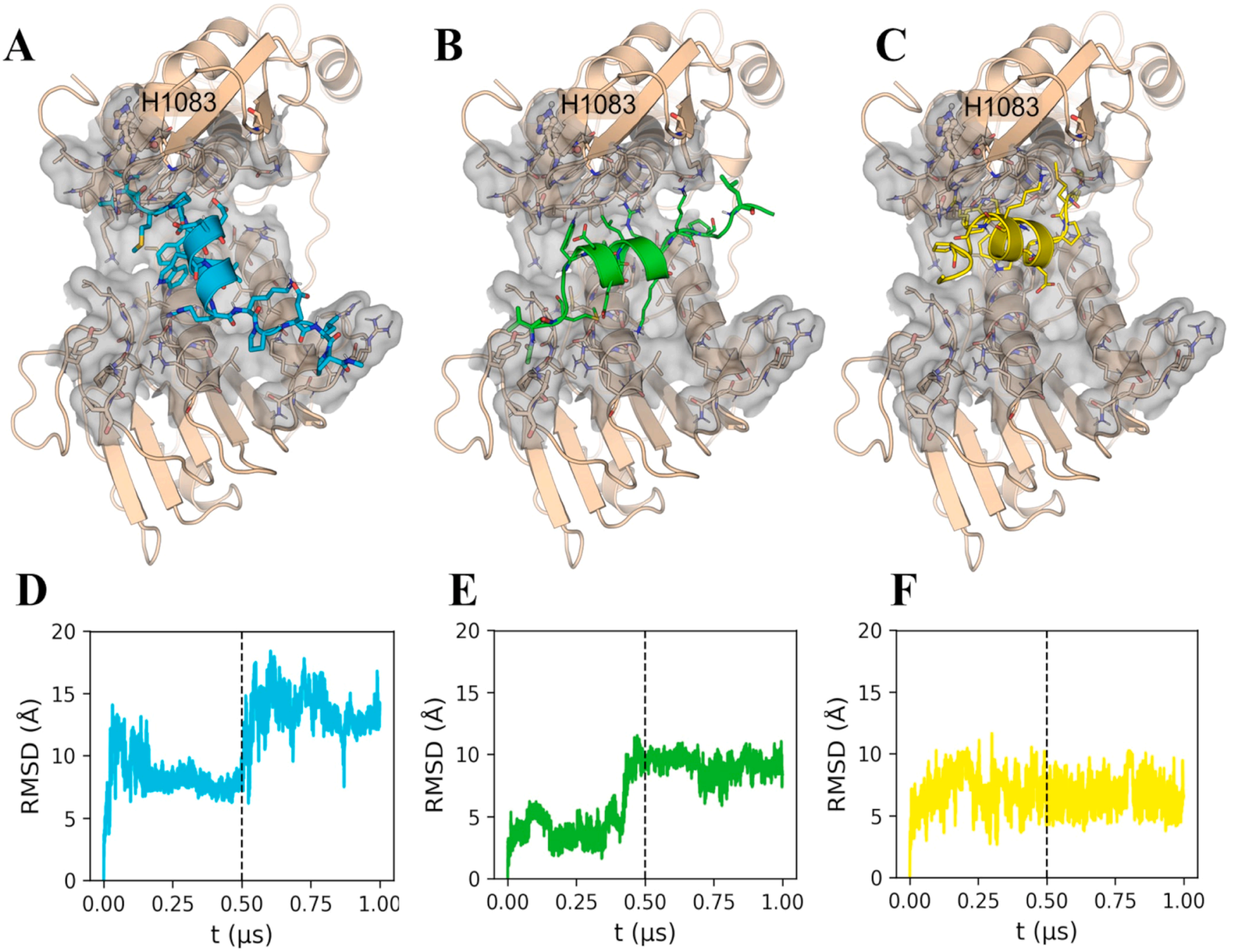

Fig. 6. Top-ranked docking poses of peptide P1 at the active site of CHIKV nsP2 protease obtained with three docking programs. (A) ClusPro, **(B)** Hdock and **(B)** Galaxy Tongdock. The peptide is colored in cyan, green or yellow depending on the program used for docking. The protein is depicted in beige, with the active site surface being colored in gray. **(D), (E)** and **(F)** show the peptide RMSD values along the MD simulations initiated with each of the docking poses shown on top. The colors of the RMSD plots match those of the peptide in the corresponding starting structure. RMSD values were calculated for the peptide's heavy atoms taking as reference the initial structure (docking pose). Prior to RMSD calculations, all trajectory frames were fitted onto the backbone atoms of the protein in the starting conformation. The dashed lines indicate that frames of the second half of each MD simulation were employed for subsequent MM-GBSA free energy calculations.

derivatives compound 10 (13.1 μM) and compound 10c (8.3 μM) (Ivanova et al., 2021). However, P1's inhibitory effect was weaker compared to RA-0,002,034 (Merten et al., 2024), which has an IC_{50} of 58 ± 17 nM. In comparison to peptide inhibitors like Pep-I (34 μM) and Pep-II (42 μM) (Singh et al., 2018) P1 demonstrated significantly greater potency, with IC_{50} values approximately tenfold lower Affinity measurements also underscore the favorable characteristics of peptide P1. The KD value of approximately 1.39 μM positions it among inhibitors with strong binding affinities. For example, P1's KD is markedly lower than that of flavonoids like hesperetin (HST) or hesperidin (HSD), further supporting its potential as an effective inhibitor of CHIKV nsP2^{pro} (Table 5).

Cytotoxicity is a crucial factor when evaluating the therapeutic potential of peptides. The MTT assay demonstrated that peptide P1, dissolved in water, exhibited low toxicity at concentrations up to 100 μM, with 77 % cell viability (Fig. 4C). However, when peptide P1 was dissolved in DMSO and subsequently diluted in DMEM medium, higher cytotoxicity was observed (Fig. 4D). Further analysis, including a DMSO titration test on Vero cells (Supplementary Fig. S10) revealed that the increased toxicity was not due to the peptide itself but rather the high concentration of DMSO. Specifically, DMSO concentrations up to 0.8 % were shown to have low toxicity. These findings are consistent with

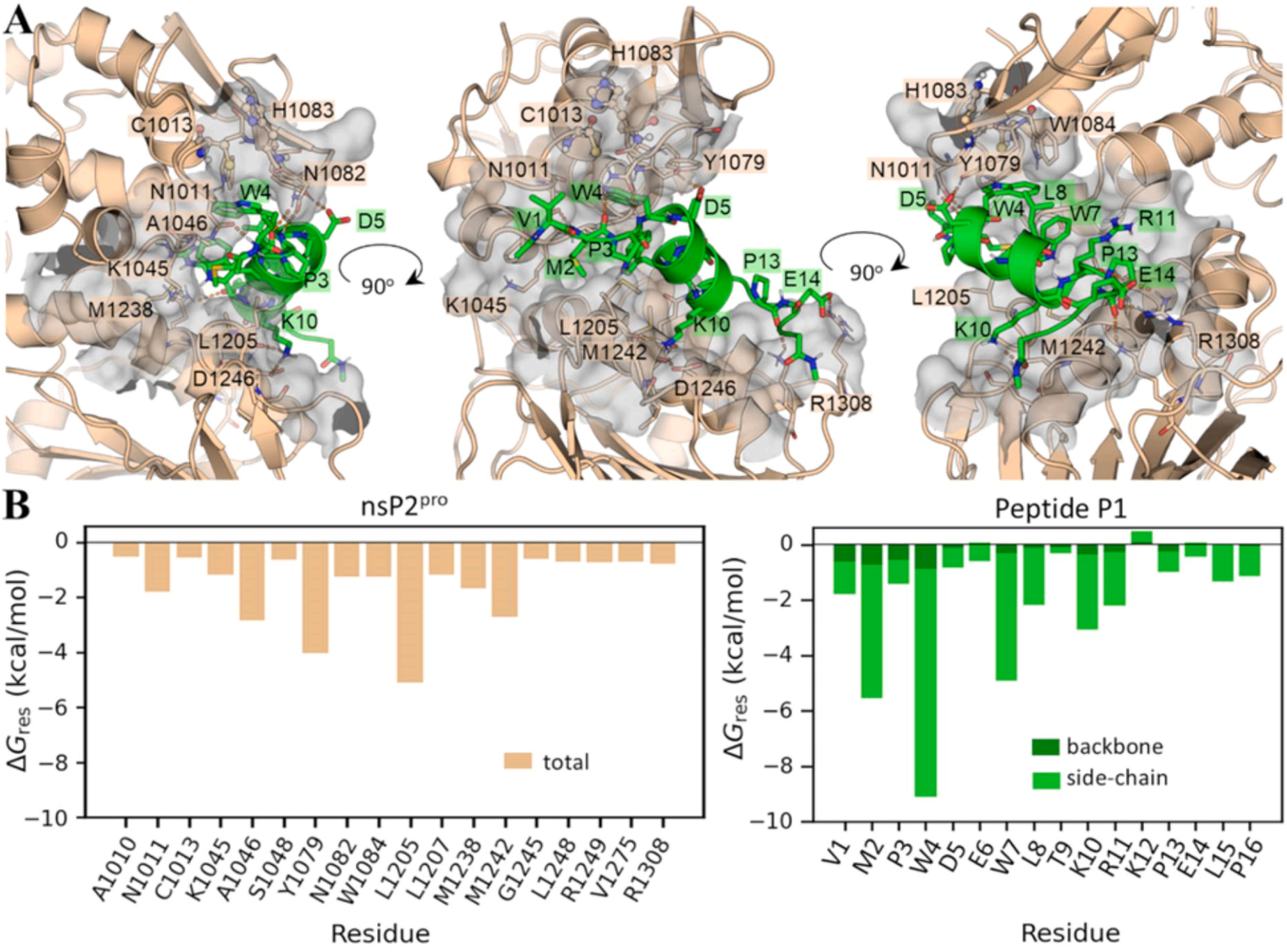

Fig. 7. Predicted binding mode of peptide P1 to CHIKV nsP2^{pro}. **(A)** Structural representation of the peptide P1 in complex with CHIKV nsP2^{pro}. Three views of the predicted complex are shown. Key interacting residues of the protein and the peptide are depicted as sticks and labeled. The active site cavity is displayed as a transparent gray surface. H-bonds at the complex interface observed during the MD simulations are represented as orange dashed lines. The central structure corresponding to the largest cluster of the 2.5 µs MD simulation was selected for representation. **(B)** Per-residue free energy (ΔG_{res}) values for warm- and hotspot residues of CHIKV nsP2^{pro} and for all residues of peptide P1. The free energy contributions of each residue side-chain and backbone are shown for the peptide.

Table 5

Inhibitors of CHIKV nsP2^{pro} reported in previous studies. The table provides an overview of the identified inhibitors, IC_{50} values, their mode of inhibition and binding affinities (if available).

Inhibitor	IC_{50} [µM]	Inhibition mode	K_D	Reference
RA-0,002,034(1)	0.058 ± 0.017	competitive	NA	(Merten et al., 2024)
1,3 Thiazolbenzamide derivatives	8.3–13.1	competitive	NA	(Ivanova et al., 2021)
Hesperetin (HST)	2.5 ± 0.4	noncompetitive	31.6 ± 2.5 µM	(Eberle et al., 2021)
Hesperidin (HSD)	7.1 ± 1.1	noncompetitive	40.7 ± 2.0 µM.	(Eberle et al., 2021)
Pep-I	34	noncompetitive	NA	(Singh et al., 2018)
Pep-II	42	competitive	NA	(Singh et al., 2018)
Novobiocin	2	NA	NA	(Tripathi et al., 2020)
Telmisarten	5	NA	NA	(Tripathi et al., 2020)

other studies, which indicate that DMSO becomes toxic at concentrations above 1 % (Aguilar et al., 2002). The differences between these studies could be attributed to variations in cell viability assessment methods. These results highlight the importance of optimizing solvent conditions to minimize toxicity in future applications. Cytotoxicity studies of other molecules, such as HST and HDT, showed that at approximately 150 µM, around 75 % of the cells remained viable (Eberle et al., 2021). A comparison suggests that P1 exhibits similar cytotoxicity, reinforcing the notion that P1 has low toxicity. Additionally, a comparison with other peptide inhibitors, such as Pep-I and Pep-II, revealed that P1 as a peptide inhibitor exhibited similar toxicity to Pep-I at 100 µM, but higher toxicity compared to Pep-II (Singh et al., 2018). To explore the structural properties of the peptides, we used I-TASSER to predict 3D structures and CD spectroscopy to determine secondary structures. Peptides P1, P3, and P5 were found to consist of a mixture of short α-helices and random coiled structures, as confirmed by their CD spectra. A typical minimum of the CD spectra between 200 and 220 nm and a maximum of around 190 nm were observed (Supplementary Fig. S8), indicative of characteristic features of α-helical structures (Haque et al., 2022). In contrast, peptides P2, P4, and P6 were determined to exhibit predominantly random coiled structures. Their CD spectra (Supplementary Fig. S8) displayed in the CD spectra a minimum of around 200 nm, which is characteristic of random coiled structures (Haque et al., 2022). The consistency between the 3D structural predictions provided by I-TASSER and the results of CD spectroscopy, as illustrated in Table S3, was used to validate the reliability of the obtained structural data. Notably, the predominantly random coil structure of peptide P4, featuring charged amino acids and exposure of hydrophobic regions, may account for its tendency to aggregate during the IC_{50} assay. This structural tendency, along with sequence differences, may also contribute to the observed variation in IC_{50} values among peptides P1, P2, and P5. Specifically, peptide P1 exhibited a higher proportion of α-helices and a lower percentage of random coil structures compared to P2 and P5. According to literature and previous studies, α-helices stabilize the protein-protein interaction and this increased structural stability can enhance their binding affinity and inhibitory effects (Wang et al., 2021). These findings suggest that peptides with a higher α-helix content are more effective inhibitors of the protease. Our molecular docking and simulation studies demonstrated that at the simulated conditions ($T = 310$ K, with protonation at pH 7.4, and $t = 20$ μs) approximately 87 % of $nsP2^{pro}$ adopts a closed and inactive conformation. Exploring the open conformations of the active site is a crucial step to investigate the binding of orthostatic ligands, especially when these ligands are relatively large, as in the present study. Our computational results reinforce previous crystallographic evidence highlighting the flexibility of the active site flap among $nsP2^{pro}$s of alphaviruses and the occurrence of an open-closure dynamics (Narwal et al., 2018). Blind docking of peptide P1, using three different approaches, consistently positioned the peptide near the active site. The stability of the predicted binding modes was thoroughly assessed by subjecting the docking poses to MD simulations and MM-GBSA free energy calculations. The most likely binding conformations of P1 were sampled during the last 2 μs of an extended MD simulation initiated from a docking pose obtained with the program HDock. The representative structure of the complex shows the peptide stretching along the open active site cavity. Further structural analyses indicated that W4, and W7 of peptide P1 interact with the critical amino acids N1011 and Y1079 at the $nsP2^{pro}$ substrate-binding sites S2 and S4 (Narwal et al., 2018). These findings align with the results from the inhibition mode assay, indicating that P1 acts as a competitive inhibitor. Per-residue free energy calculations identified W4 as the primary hotspot residue in the peptide, with a side-chain ΔG_{res} values of −8.2 kcal/mol, followed by M2 (−4.8 kcal/mol) and W7 (−4.6 kcal/mol). These findings highlight the critical role of these three amino acid residues in the binding of peptide P1. Understanding the energy contribution of each residue is essential for optimizing and modifying the peptide to improve its binding affinity to the protease. Redesign strategies should prioritize mutations at these hotspot positions to explore potential improvements. Additionally, future studies also evaluate the specificity of peptide P1 against the CHIKV $nsP2^{pro}$.

5. Conclusion and future perspectives

In this study, six peptides were identified as potential binders of the CHIKV $nsP2^{pro}$ through phage display, with peptide P1 exhibiting the highest inhibitory activity. Peptide P1 showed a competitive inhibition mode, with an IC_{50} of 4.6 μM and K_D of approximately 1.39 μM, indicating strong binding affinity for its target. Structural and cytotoxicity analyses further emphasized P1′s therapeutic potential; however, solvent optimization is essential to mitigate DMSO-related toxicity. Molecular docking studies confirmed P1′s binding to essential substrate-binding sites of $nsP2^{pro}$, highlighting the importance of key residues in inhibitor-protease interactions.

Funding

MM thanks Jürgen Manchot Stiftung for providing financial assistance and resources. JEHG thanks the financial support of the National Council for Scientific and Technological Development (CNPq), Grant 153794/2024-0, and of the Sao Paulo Research Foundation (FAPESP), Grants 2022/03901-8, 2024/13327-2 and 2020/08615-8.

Declaration of generative AI and AI-assisted technologies in the writing process

ChatGPT was used to check grammar and spelling in order to improve readability. After using this tool, the authors reviewed and edited the content and take full responsibility for the content of the publication. Part of the figures were created by BioRender program.

CRediT authorship contribution statement

Mohammadamin Mastalipour: Conceptualization, Methodology, Formal analysis, Data curation, Writing – original draft, Writing – review & editing. **Ian Gering:** Methodology, Formal analysis, Writing – original draft, Writing – review & editing. **Mônika Aparecida Coronado:** Supervision, Formal analysis, Writing – original draft, Writing – review & editing. **Jorge Enrique Hernández González:** Methodology, Formal analysis, Data curation, Writing – original draft, Writing – review & editing. **Dieter Willbold:** Resources, Writing – original draft, Writing – review & editing. **Raphael Josef Eberle:** Conceptualization, Formal analysis, Supervision, Writing – original draft, Writing – review & editing.

Declaration of competing interest

The authors declare that they have no known competing financial interests or personal relationships that could have appeared to influence the work reported in this paper.

Acknowledgements

We would like to express our sincere gratitude to Jürgen Manchot Stiftung for providing financial assistance and resources that were critical to the success of this project. JEHG thanks the National Laboratory for Scientific Computing (LNCC/MCTI, Brazil) for providing HPC resources of the SDumont supercomputer, URL: http://sdumont.lncc.br.

Supplementary materials

Supplementary material associated with this article can be found, in the online version, at doi:10.1016/j.crmicr.2025.100376.

Data availability

All relevant data are included in this manuscript and its supporting information. Further inquiries or requests for materials can be directed to eberler@hhu.de.

References

Aguilar, J.S., Roy, D., Ghazal, P., Wagner, E.K., 2002. Dimethyl sulfoxide blocks herpes simplex virus-1 productive infection *in vitro* acting at different stages with positive cooperativity. Application of micro-array analysis. BMC Infect. Dis. 2. https://doi.org/10.1186/1471-2334-2-9.

Ahmed, S., Sultana, S., Kundu, S., Alam, S.S., Hossan, T., Islam, M.A., 2024. Global prevalence of Zika and Chikungunya coinfection: a systematic review and meta-analysis. Diseases 12 (2). https://doi.org/10.3390/diseases12020031.

Alfaleh, M.A., Alsaab, H.O., Mahmoud, A.B., Alkayyal, A.A., Jones, M.L., Mahler, S.M., & Hashem, A.M. (2020). Phage display derived monoclonal antibodies: from bench to bedside. https://doi.org/10.3389/fimmu.2020.01986.

Altendorf, T., Mohrlüder, J., Willbold, D., 2024. TSAT: efficient evaluation software for NGS data of phage/mirror-image phage display selections. Biophys. Rep. 4 (3). https://doi.org/10.1016/j.bpr.2024.100166 (N. Y).

Blat, Y., 2010. Non-competitive inhibition by active site binders. Chem. Biol. Drug Des. 75 (6), 535–540. https://doi.org/10.1111/j.1747-0285.2010.00972.x.

Case, D.A., Cheatham III, T.E., Darden, T., Gohlke, H., Luo, R., Merz Jr., K.M., Onufriev, A., Simmerling, C., Wang, B., Woods, R.J., 2005. The Amber biomolecular simulation programs. J. Comput. Chem. 26 (16), 1668–1688.

Chen, L.H., Fritzer, A., Hochreiter, R., Dubischar, K., Meyer, S., 2024. From bench to clinic: the development of VLA1553/IXCHIQ, a live-attenuated Chikungunya vaccine. J. Travel. Med. 31 (7). https://doi.org/10.1093/jtm/taae123.

Da Silva Ribeiro, A.C., de Carvalho, C.A.M., Casseb, S.M.M., Rodrigues, S.G., da Costa Vasconcelos, P.F., Carvalho, V.L, 2018. Infection profiles of Mayaro virus and Chikungunya virus in mammalian and mosquito cell lineages. Rev. Pan-Amaz. Saúde 9 (4), 11. http://doi.org/10.5123/s2176-62232018000400003.

Delrieu, M., Martinet, J.P., O'Connor, O., Viennet, E., Menkes, C., Burtet-Sarranmegna, V., Dupont-Rouzeyrol, M., 2023. Temperature and transmission of Chikungunya, dengue, and Zika viruses: a systematic review of experimental studies on Aedes aegypti and Aedes albopictus. Curr. Res. Parasitol. Vector-Borne Dis. 4. https://doi.org/10.1016/j.crpvbd.2023.100139.

De Souza, W.M., Ribeiro, G.S., de Lima, S.T.S., de Jesus, R., Moreira, F.R.R., Whittaker, C., Sallum, M.A.M., Carrington, C.V.F., Sabino, E.C., Kitron, U., Faria, N. R., Weaver, S.C., 2024. Chikungunya: a decade of burden in the Americas. Lancet Reg. Health Am. 30, 100673. https://doi.org/10.1016/j.lana.2023.100673 (Engl. ed).

Dolinsky, T.J., Nielsen, J.E., McCammon, J.A., Baker, N.A., 2004. PDB2PQR: an automated pipeline for the setup of Poisson–Boltzmann electrostatics calculations. Nucleic Acids Res. 32 (suppl_2), W665–W667. https://doi.org/10.1093/nar/gkh381.

Eberle, R.J., Olivier, D.S., Pacca, C.C., Avilla, C.M.S., Nogueira, M.L., Amaral, M.S., Coronado, M.A., 2021. study of Hesperetin and Hesperidin as inhibitors of Zika and Chikungunya virus proteases. PLoS One 16 (3). https://doi.org/10.1371/journal.pone.0246319.

Eberle, R.J., Sevenich, M., Gering, I., Scharbert, L., Strodel, B., Lakomek, N.A., Willbold, D., 2023. Discovery of all-D-peptide inhibitors of SARS-CoV-2 3C-like protease. ACS Chem. Biol. 18 (2), 315–330. https://doi.org/10.1021/acschembio.2c00735.

El-Sayed, A., Kamel, M., 2020. Climatic changes and their role in emergence and re-emergence of diseases. Environ. Sci. Pollut. Res. 27 (18), 22336–22352. https://doi.org/10.1007/s11356-020-08896-w.

European Centre for Disease Prevention and Control, 2024. Chikungunya Worldwide Overview. December 17. ECDC. https://www.ecdc.europa.eu/en/chikungunya-monthly.

Freppel, W., Silva, L.A., Stapleford, K.A., Herrero, L.J., 2024. Pathogenicity and virulence of Chikungunya virus. Virulence 15 (1). https://doi.org/10.1080/21505594.2024.2396484.

Ghoshal, A., Asressu, K.H., Hossain, M.A., Brown, P.J., Nandakumar, M., Vala, A., Willson, T.M., 2024. Structure activity of beta-amidomethyl vinyl sulfones as covalent inhibitors of Chikungunya nsP2 cysteine protease with antialphavirus activity. J. Med. Chem. 67 (18), 16505–16532. https://doi.org/10.1021/acs.jmedchem.4c01346.

Girard, J., Le Bihan, O., Lai-Kee-Him, J., Girleanu, M., Bernard, E., Castellarin, C., Bron, P., 2024. In situ fate of Chikungunya virus replication organelles. J. Virol. 98 (7), e0036824. https://doi.org/10.1128/jvi.00368-24.

Göertz, G.P., McNally, K.L., Robertson, S.J., Best, S.M., Pijlman, G.P., Fros, J.J., 2018. The methyltransferase-like domain of Chikungunya virus nsP2 inhibits the interferon response by promoting the nuclear export of STAT1. J. Virol. 92 (17). https://doi.org/10.1128/jvi.01008-18.

Grabenstein, J.D., Tomar, A.S., 2023. Global geotemporal distribution of Chikungunya disease, 2011-2022. Travel Med. Infect. Dis. 54. https://doi.org/10.1016/j.tmaid.2023.102603.

Haque, M.A., Kaur, P., Islam, A., Hassan, M.I., 2022. Chapter 14 - application of circular dichroism spectroscopy in studying protein folding, stability, and interaction (Eds.). In: Tripathi, T., Dubey, V.K. (Eds.), Advances in Protein Molecular and Structural Biology Methods. Academic Press, pp. 213–224. https://doi.org/10.1016/B978-0-323-90264-9.00014-3.

Hopkins, C.W., Le Grand, S., Walker, R.C., Roitberg, A.E., 2015. Long-time-step molecular dynamics through hydrogen mass repartitioning. J. Chem. Theory Comput. 11 (4), 1864. https://doi.org/10.1021/ct5010406.

Hu, X., Compton, J.R., Leary, D.H., Olson, M.A., Lee, M.S., Cheung, J., Legler, P.M., 2016. Kinetic, mutational, and structural studies of the Venezuelan Equine Encephalitis virus nonstructural protein 2 cysteine protease. Biochemistry 55 (21), 3007–3019. https://doi.org/10.1021/acs.biochem.5b00992.

Ivanova, L., Rausalu, K., Zusinaite, E., Tammiku-Taul, J., Merits, A., Karelson, M., 2021. 1,3-Thiazolbenzamide derivatives as Chikungunya virus nsP2 protease inhibitors. ACS Omega 6 (8), 5786–5794. https://doi.org/10.1021/acsomega.0c06191.

Izadi, S., Anandakrishnan, R., Onufriev, A.V., 2014. Building water models: a different approach. J. Phys. Chem. Lett. 5 (21), 3863–3871. https://doi.org/10.1021/jz501780a.

Jadav, S.S., Sinha, B.N., Hilgenfeld, R., Pastorino, B., de Lamballerie, X., Jayaprakash, V., 2015. Thiazolidone derivatives as inhibitors of Chikungunya virus. Eur. J. Med. Chem. 89, 172–178. https://doi.org/10.1016/j.ejmech.2014.10.042.

Jerabek-Willemsen, M., André, T., Wanner, R., Roth, H.M., Duhr, S., Baaske, P., Breitsprecher, D., 2014. MicroScale thermophoresis: interaction analysis and beyond. J. Mol. Struct. 1077, 101–113. https://doi.org/10.1016/j.molstruc.2014.03.009.

Jones, G., Jindal, A., Ghani, U., Kotelnikov, S., Egbert, M., Hashemi, N., Kozakov, D., 2022. Elucidation of protein function using computational docking and hotspot analysis by ClusPro and FTMap. Acta Crystallogr. D 78 (6), 690–697. https://doi.org/10.1107/S2059798322002741.

Khongwichit, S., Chuchaona, W., Vongpunsawad, S., Poovorawan, Y., 2022. Molecular surveillance of arboviruses circulation and co-infection during a large Chikungunya virus outbreak in Thailand, October 2018 to February 2020. Sci. Rep. 12 (1). https://doi.org/10.1038/s41598-022-27028-7.

Kutzsche, J., Jürgens, D., Willuweit, A., Adermann, K., Fuchs, C., Simons, S., Willbold, D., 2020. Safety and pharmacokinetics of the orally available antiprionic compound PRI-002: a single and multiple ascending dose phase I study. (New York, N. Y.) 6 (1), e12001. https://doi.org/10.1002/trc2.12001.

Law, Y.S., Wang, S., Tan, Y.B., Shih, O., Utt, A., Goh, W.Y., Lian, B.J., et al., 2021. Interdomain flexibility of chikungunya virus nsP2 helicase-protease differentially influences viral RNA replication and infectivity. J. Virol. 95 (6), 10–1128.

Ly, H., 2024. Ixchiq (VLA1553): the first FDA-approved vaccine to prevent disease caused by Chikungunya virus infection. Virulence 15 (1). https://doi.org/10.1080/21505594.2023.2301573.

Marimoutou, C., Ferraro, J., Javelle, E., Deparis, X., Simon, F., 2015. Chikungunya infection: self-reported rheumatic morbidity and impaired quality of life persist 6 years later. Clin. Microbiol. Infect. 21 (7), 688–693. https://doi.org/10.1016/j.cmi.2015.02.024.

Martins, D.O.S., Ruiz, U.E.A., Santos, I.A., Oliveira, I.S., Guevara-Vega, M., de Paiva, R.E. F., Jardim, A.C.G., 2024. Exploring the antiviral activities of the FDA-approved drug sulfadoxine and its derivatives against Chikungunya virus. Pharmacol. Rep. 76 (5), 1147–1159. https://doi.org/10.1007/s43440-024-00635-z.

Mayer, S.V., Tesh, R.B., Vasilakis, N., 2017. The emergence of arthropod-borne viral diseases: a global prospective on dengue, Chikungunya and Zika fevers. Acta Trop. 166, 155–163. https://doi.org/10.1016/j.actatropica.2016.11.020.

Merten, E.M., Sears, J.D., Leisner, T.M., Hardy, P.B., Ghoshal, A., Hossain, M.A., Pearce, K.H., 2024. Identification of a cell-active Chikungunya virus nsP2 protease inhibitor using a covalent fragment-based screening approach. Proc. Natl. Acad. Sci. U. S. A. 121 (42), e2409166121. https://doi.org/10.1073/pnas.2409166121.

Miller 3rd, B.R., McGee Jr., T.D., Swails, J.M., Homeyer, N., Gohlke, H., Roitberg, A.E., 2012. MMPBSA.py: an efficient program for end-state free energy calculations. J. Chem. Theory Comput. https://doi.org/10.1021/ct300418h.

Mourad, O., Makhani, L., Chen, L.H., 2022. Chikungunya: an emerging public health concern. Curr. Infect. Dis. Rep. 24 (12), 217–228. https://doi.org/10.1007/s11908-022-00789-y.

Narwal, M., Singh, H., Pratap, S., Malik, A., Kuhn, R.J., Kumar, P., Tomar, S., 2018. Crystal structure of Chikungunya virus nsP2 cysteine protease reveals a putative flexible loop blocking its active site. Int. J. Biol. Macromol. 116, 451–462. https://doi.org/10.1016/j.ijbiomac.2018.05.007.

Nguyen, H., Roe, D.R., Simmerling, C., 2013. Improved generalized born solvent model parameters for protein simulations. J. Chem. Theory Comput. 9 (4), 2020–2034. https://doi.org/10.1021/ct3010485.

Paixao, E.S., Rodrigues, L.C., Costa, M.D.N., Itaparica, M., Barreto, F., Gérardin, P., Teixeira, M.G., 2018. Chikungunya chronic disease: a systematic review and meta-analysis. Trans. R. Soc. Trop. Med. Hyg. 112 (7), 301–316. https://doi.org/10.1093/trstmh/try063.

Park, T., Baek, M., Lee, H., Seok, C., 2019. GalaxyTongDock: symmetric and asymmetric ab initio protein–protein docking web server with improved energy parameters. J. Comput. Chem. 40 (27), 2413–2417. https://doi.org/10.1002/jcc.25874.

Peinado, R.D.S., Eberle, R.J., Arni, R.K., Coronado, M.A., 2022. A review of omics studies on Arboviruses: Alphavirus, Orthobunyavirus and Phlebovirus. Viruses 14 (10), 2194. https://doi.org/10.3390/v14102194.

Peinado, R.D.S., Martins, L.G., Pacca, C.C., Saivish, M.V., Borsatto, K.C., Nogueira, M.L., Coronado, M.A., 2024. HR-MAS NMR metabolomics profile of vero cells under the influence of virus infection and nsP2 inhibitor: a Chikungunya case study. Int. J. Mol. Sci. 25 (3). https://doi.org/10.3390/ijms25031414.

Rama, K., de Roo, A.M., Louwsma, T., Hofstra, H.S., do Amaral, G.S.G., Vondeling, G.T., Freriks, R.D., 2024. Clinical outcomes of Chikungunya: a systematic literature review and meta-analysis. PLoS Negl. Trop. Dis. 18 (6). https://doi.org/10.1371/journal.pntd.0012254.

Rawlings, N.D., Barrett, A.J., Bateman, A., 2010. MEROPS: the peptidase database. Nucleic Acids Res. 38 (suppl_1), D227–D233.

Rossotti, M.A., Trempe, F., van Faassen, H., Hussack, G., Arbabi-Ghahroudi, M., 2023. Isolation and characterization of single-domain antibodies from immune phage display libraries. Methods Mol. Biol. 2702, 107–147. https://doi.org/10.1007/978-1-0716-3381-6_7 (Clifton, N.J.).

Schneider, M., Narciso-Abraham, M., Hadl, S., Mcmahon, R., Toepfer, S., Fuchs, U., Wressnigg, N., 2023. Safety and immunogenicity of a single-shot live-attenuated Chikungunya vaccine: a double-blind, multicentre, randomised, placebo-controlled, phase 3 trial. Lancet 401 (10394), 2138–2147. https://doi.org/10.1016/S0140-6736(23)00641-4.

Sevenich, M., Thul, E., Lakomek, N.A., Kluenemann, T., Schubert, M., Bertoglio, F., Willbold, D., 2022. Phage display-derived compounds displace hACE2 from its complex with SARS-CoV-2 spike protein. Biomedicines 10 (2). https://doi.org/10.3390/biomedicines10020441.

Sharif, N., Sarkar, M.K., Ferdous, R.N., Ahmed, S.N., Billah, M.B., Talukder, A.A., Dey, S. K., 2021. Molecular epidemiology, evolution and reemergence of Chikungunya virus in South Asia. Front. Microbiol. 12. https://doi.org/10.3389/fmicb.2021.689979.

Silva, L.A., Dermody, T.S., 2017. Chikungunya virus: epidemiology, replication, disease mechanisms, and prospective intervention strategies. J. Clin. Investig. 127 (3), 737–749. https://doi.org/10.1172/Jci84417.

Simon, F., Javelle, E., Oliver, M., Leparc-Goffart, I., Marimoutou, C., 2011. Chikungunya virus infection. Curr. Infect. Dis. Rep. 13 (3), 218–228. https://doi.org/10.1007/s11908-011-0180-1.

Singh, H., Mudgal, R., Narwal, M., Kaur, R., Singh, V.A., Malik, A., Tomar, S., 2018. Chikungunya virus inhibition by peptidomimetic inhibitors targeting virus-specific cysteine protease. Biochimie 149, 51–61. https://doi.org/10.1016/j.biochi.2018.04.004.

Solignat, M., Gay, B., Higgs, S., Briant, L., Devaux, C., 2009. Replication cycle of Chikungunya: a re-emerging arbovirus. Virology 393 (2), 183–197. https://doi.org/10.1016/j.virol.2009.07.024.

Tian, C., Kasavajhala, K., Belfon, K.A.A., Raguette, L., Huang, H., Migues, A.N., Simmerling, C., 2020. ff19SB: amino-acid-specific protein backbone parameters trained against quantum mechanics energy surfaces in solution. J. Chem. Theory Comput. 16 (1), 528–552. https://doi.org/10.1021/acs.jctc.9b00591.

Tripathi, P.K., Soni, A., Singh Yadav, S.P., Kumar, A., Gaurav, N., Raghavendhar, S., Patel, A.K., 2020. Evaluation of novobiocin and telmisartan for anti-CHIKV activity. Virology 548, 250–260. https://doi.org/10.1016/j.virol.2020.05.010.

van Groen, T.A.-O., Schemmert, S., Brener, O., Gremer, L., Ziehm, T., Tusche, M., Willbold, D.A.-O., 2017. The Aβ oligomer eliminating D-enantiomeric peptide RD2 improves cognition without changing plaque pathology. Sci. Rep. 7 (1), 16275. https://doi.org/10.1038/s41598-017-16565-1.

Vikhe, V.B., Faruqi, A.A., Reddy, A., Khandol, D., Lapsiwala, V.H., 2023. Dengue and Chikungunya Co-infection- associated multi-organ dysfunction syndrome: a case report. Cureus J. Med. Sci. 15 (12). https://doi.org/10.7759/cureus.50196.

Wang, H., Dawber, R.S., Zhang, P., Walko, M., Wilson, A.J., Wang, X., 2021. Peptide-based inhibitors of protein-protein interactions: biophysical, structural and cellular consequences of introducing a constraint. Chem. Sci. 12 (17), 5977–5993. https://doi.org/10.1039/d1sc00165e.

Ware, B.C., Parks, M.G., da Silva, M.O.L., Morrison, T.E., 2024. Chikungunya virus infection disrupts MHC-I antigen presentation via nonstructural protein 2. PLoS Pathog. 20 (3). https://doi.org/10.1371/journal.ppat.1011794.

Yan, Y., Tao, H., He, J., Huang, S.-Y., 2020. The HDOCK server for integrated protein–protein docking. Nat. Protoc. 15 (5), 1829–1852. https://doi.org/10.1038/s41596-020-0312-x.

Yang, J.Y., Yan, R.X., Roy, A., Xu, D., Poisson, J., Zhang, Y., 2015. The I-TASSER suite: protein structure and function prediction. Nat. Methods 12 (1), 7–8. https://doi.org/10.1038/nmeth.3213.

Yau, A.W.N., Chu, S.Y.C., Yap, W.H., Wong, C.L., Chia, A.Y.Y., Tang, Y.Q., 2024. Phage display screening in Breast Cancer: from peptide discovery to clinical applications. Life Sci. 357, 123077. https://doi.org/10.1016/j.lfs.2024.123077.

Zaid, A., Gérardin, P., Taylor, A., Mostafavi, H., Malvy, D., Mahalingam, S., 2018. Chikungunya arthritis implications of acute and chronic inflammation mechanisms on disease management. Arthritis Rheumatol. 70 (4), 484–495. https://doi.org/10.1002/art.40403.

Zhou, X., Zheng, W., Li, Y., Pearce, R., Zhang, C., Bell, E.W., Zhang, G., Zhang, Y., 2022. I-TASSER-MTD: a deep-learning-based platform for multi-domain protein structure and function prediction. Nat. Protoc. 17 (10), 2326–2353. https://doi.org/10.1038/s41596-022-00728-0.